



Highly efficient photocatalytic degradation of naphthalene by $\text{Co}_3\text{O}_4/\text{Bi}_2\text{O}_2\text{CO}_3$ under visible light: A novel p–n heterojunction nanocomposite with nanocrystals/lotus-leaf-like nanosheets structure

Yang Guo^{a,c}, Yuxuan Dai^a, Wei Zhao^b, Hui Li^c, Bin Xu^d, Cheng Sun^{a,*}

^a State Key Laboratory of Pollution Control and Resource Reuse, School of the Environment, Nanjing University, Nanjing 210023, PR China

^b Department of Mechanical Engineering, University of Hong Kong, Pokfulam Road, Hong Kong, PR China

^c Department of Plant, Soil and Microbial Sciences, Plant and Soil Science Building, 1066 Bogue Street Michigan State University East Lansing, Michigan 48824, United States

^d State Key Laboratory of Pollution Control and Resource Reuse, College of Environmental Science and Engineering, Tongji University, Shanghai, 200092, PR China

ARTICLE INFO

Keywords:

$\text{p-Co}_3\text{O}_4/\text{n-Bi}_2\text{O}_2\text{CO}_3$
Nanocrystals/lotus-leaf-like nanosheets
p–n heterojunction
Photocatalytic mechanism
Photodegradation pathways
Naphthalene

ABSTRACT

Exploring visible-light-driven nanomaterials to substitute crucial bulk composite under UV-light is of great significance in photodegradation of hardly-decomposed persistent pollutants in the environment. Herein, the novel p–n heterojunction photocatalyst $\text{p-Co}_3\text{O}_4/\text{n-Bi}_2\text{O}_2\text{CO}_3$ with zero dimensional(0D)-two dimensional(2D) nanocrystals/lotus-leaf-like nanosheets structure was successfully obtained for the first time via a facile hydrothermal method, in which the density of Co_3O_4 loaded on the $\text{Bi}_2\text{O}_2\text{CO}_3$ was easily tuned by the concentration of Co_3O_4 precursor in the solution. The outstanding feature of the photocatalyst is that the resultant hybrid nanocomposite exemplified the p–n heterojunction visible-light materials for degrading the naphthalene efficiently and effectively. As the presence of Co_3O_4 and the synergistic interactions of p–n heterojunction, the recombination of photogenerated charge carriers has been suppressed, and the visible light absorbance has been improved. Consequently, the visible light photocatalytic performance has been enhanced. The $\text{p-Co}_3\text{O}_4/\text{n-Bi}_2\text{O}_2\text{CO}_3$ sample with $\text{Co}_3\text{O}_4/\text{Bi}_2\text{O}_2\text{CO}_3$ mass ratio 1:6 exhibited the highest photocatalytic activities among all the as-prepared samples with the degradation efficiency of about 91.02% naphthalene in 150 min. The photocatalytic mechanism of $\text{p-Co}_3\text{O}_4/\text{n-Bi}_2\text{O}_2\text{CO}_3$ for degrading naphthalene was analyzed based on the semiconductor energy band theory and the formation of an internal electrostatic field. The probable degradation intermediates and products of naphthalene were identified by GC–MS. The proposed photodegradation pathways of naphthalene were described by combining the frontier electron density calculation and GC–MS results.

1. Introduction

Nowadays, environmental pollution has been deteriorating along with the rapid development of the economy and energy shortages also remain the serious problem for the potential global crisis. Among the environmental issues, pollution of polycyclic aromatic hydrocarbons (PAHs) creates the major focus of the world attention, because their distribution and exposure in the environment should pose the threat to human health [1]. They are considered as hazardous pollutants due to their toxicity, mutagenicity, and carcinogenicity and are classified as persistent organic pollutants that are ubiquitous in the environment [2,3]. All PAHs are neutral and nonpolar compounds, which have high stability and are difficult to be degraded. However, all environmental compartments, such as air, soil, water, and biota can find PAHs which

are introduced into the environment via natural and anthropogenic activities [4–6]. Therefore, effective methods to eliminate PAHs are urgently needed to result in no further harm to humans and reduction of potential environmental problems.

Semiconductor photocatalysis, as a kind of green technology for environmental remediation, received more attention in the past few years, meanwhile gained extensive research and application due to its potential utilization of solar energy for purification of water and air [7]. Unfortunately, traditional semiconductor photocatalysts (TiO_2 , ZnO , etc.) which have been proved to be the most representative ones, are limited to get the adsorption under solar radiation, since they only adsorb UV light which is only 3–5% in the whole solar light. It greatly restricts their practical applications [8,9]. Therefore, many efforts have been devoted to developing the novel photocatalysts with the high

* Corresponding author.

E-mail address: envidan@nju.edu.cn (C. Sun).

<https://doi.org/10.1016/j.apcatb.2018.05.089>

Received 13 February 2018; Received in revised form 1 May 2018; Accepted 30 May 2018
Available online 30 May 2018

0926-3373/ © 2018 Elsevier B.V. All rights reserved.

photocatalytic performances, like BiVO_4 [10–12], $\text{Bi}_4\text{O}_5\text{Br}_2$ [13–15], $\text{Bi}_2\text{O}_2\text{CO}_3$ [16,17], $\text{g-C}_3\text{N}_4$ [18,19] and so on. Among these new materials, it is significant to find that bismuth subcarbonate ($\text{Bi}_2\text{O}_2\text{CO}_3$) is one of the most attractive candidate owing to its low mammalian toxicity for medical treatment, which has long been used for the healthcare purpose and its photocatalytic performance of degrading pollutants due to its band gap being 2.87–3.55 eV [20,21]. It is a typical “sillén” phase bearing a resemblance to the Aurivillius oxides, in which $\text{Bi}_2\text{O}_2^{2+}$ layers and CO_3^{2-} layers are interlayered with the plane of the CO_3^{2-} group orthogonal to the plane of the $\text{Bi}_2\text{O}_2^{2+}$ layer [22]. Since Cheng et al. [23] first reported the application of hierarchical flower-like microstructure $\text{Bi}_2\text{O}_2\text{CO}_3$ as a photocatalyst for degradation of methyl orange under UV light. The subsequent researches about the photocatalytic performance with various morphologies of $\text{Bi}_2\text{O}_2\text{CO}_3$ have been focused. Liu et al. [24] prepared the irregular nanosheets using the hydrothermal and solvothermal method to investigate the photocatalytic performance by decolorizing RhB and decomposing 2-propanol under UV–vis light irradiation, and demonstrated that $\text{Bi}_2\text{O}_2\text{CO}_3$ had potential application in environmental remediation process. Zheng et al. [25] also synthesized the nanostructure $\text{Bi}_2\text{O}_2\text{CO}_3$ with flower-like, sponge-like and plate-like morphologies and demonstrated that the different structure of $\text{Bi}_2\text{O}_2\text{CO}_3$ might impact on the photocatalytic ability.

However, there have been no reports about the lotus-leaf-like 2D nanosheet structure of $\text{Bi}_2\text{O}_2\text{CO}_3$ yet. Moreover, although Zhao et al. [20] found that as-prepared sponge-like $\text{Bi}_2\text{O}_2\text{CO}_3$ microspheres owned a narrowed band gap of 2.87 eV and exhibited a powerful visible-light-photocatalytic activity for the degradation of dyes, common $\text{Bi}_2\text{O}_2\text{CO}_3$ photocatalysts could mainly absorb UV light due to their wide band gap, and also have the low ability of separation of photogenerated electron-hole pairs, which greatly limit their practical applications [26]. Thus, further study is necessary to enhance the photocatalytic efficiency under visible light.

The formation of heterojunction between composite semiconductor catalysts is one of the most sensible approaches to improve the visible light responsible ability and potentially act to suppress the recombination of charge carriers [27–29]. A number of $\text{Bi}_2\text{O}_2\text{CO}_3$ -based heterojunction photocatalysts such as $\text{Bi}_2\text{S}_3/\text{Bi}_2\text{O}_2\text{CO}_3$ [30], $\text{BiVO}_4/\text{Bi}_2\text{O}_2\text{CO}_3$ [16], $\text{g-C}_3\text{N}_4/\text{Bi}_2\text{O}_2\text{CO}_3$ [31] have been investigated in the past decade. For example, Liang et al. [32] have obtained $\text{Ag}_2\text{O}/\text{Bi}_2\text{O}_2\text{CO}_3$ p–n heterojunctions, which show higher photocatalytic activity than that of pure n- $\text{Bi}_2\text{O}_2\text{CO}_3$, and the composites exhibit the high photocatalytic performance under visible light ($\lambda > 400$ nm) for the degradation of Rhodamine B, methyl blue and methyl orange within 12 min. Yu et al. [33] have successfully developed the highly efficient photocatalyst of $\text{Bi}_2\text{O}_2\text{CO}_3/\text{BiOCl}$. The photocatalytic activity of the composite $\text{Bi}_2\text{O}_2\text{CO}_3/\text{BiOCl}$ toward Rhodamine B (RhB) under visible light is even better than that of P25 (commercial TiO_2) under UV light. These researchers reveal that combining $\text{Bi}_2\text{O}_2\text{CO}_3$ with other semiconductor photocatalysts which have the lower and matched band gap is a promising method to achieve the separation of electron-hole pairs, thereby possessing better performance than that of a single one.

Generally, cobalt oxide (Co_3O_4) has been intensively explored as a p-type semiconductor with a narrow band gap and its possible application owing to the interesting electronic, photochemical and magnetic properties [34–36]. Co_3O_4 has been widely used in various fields, for example, it is intrinsically active for CO oxidation in low-temperature [37]; it is evaluated as semiconductor catalysts to effectively reduce CO_2 to carbon-based products under visible light [29]; and it is suitable as negative electrodes for next-generation lithium ion batteries [38]. Recently, Long et al. [39] reported the p–n heterojunction $\text{Co}_3\text{O}_4/\text{BiVO}_4$ photocatalysts showed superior performance for the degradation of phenol under visible light irradiation, which could be explained by the formation of p–n heterojunction semiconductor structure. The applications of Co_3O_4 as photocatalysts in the water remediation have been broadly concerned. Han et al. [40] fabricated the novel visible-

light-induced Co_3O_4 -g- C_3N_4 heterojunction photocatalysts via a facile mixing-heating method, showing the enhanced photocatalytic activity because of the presence of Co_3O_4 which inhibits the recombination of electron-hole pairs. These studies have demonstrated that Co_3O_4 has a magnificent potential applied in the field of photocatalysis to enhance the photocatalytic performance.

According to the preceding discussion, we proposed the hypothesis that the effective charge transfer of heterojunction may be in favor of improving the photocatalytic performance. In order to verify this hypothesis, the nanocrystals Co_3O_4 loaded on the lotus-leaf-like 2D nanosheets $\text{Bi}_2\text{O}_2\text{CO}_3$ were conducted for the first time via a hydrothermal method in this study. Furthermore, Co_3O_4 and $\text{Bi}_2\text{O}_2\text{CO}_3$ are intrinsic p-type and n-type semiconductor, respectively. Theoretically, a p–n heterojunction will be formed when the p-type Co_3O_4 and the n-type $\text{Bi}_2\text{O}_2\text{CO}_3$ successfully integrate. The p–n heterojunction could provide a concentration difference between charges, leading to the formation of an internal electric field, with its field direction from the n-type to the p-type semiconductor. However, to our best knowledge, the preparation and properties of the p–n heterojunction photocatalyst $\text{Co}_3\text{O}_4/\text{Bi}_2\text{O}_2\text{CO}_3$ with 0D-2D structure has not been reported yet. Compared with bulk materials, 0D nanomaterials are to the benefit of the rapid migration of photogenerated electrons and holes from the inner part to the surface because of the tiny particle size. 2D nanosheets generally possess many extraordinary properties, such as high specific surface area and outstanding electronic conductivity [41]. It is purposed that the 0D-2D $\text{Co}_3\text{O}_4/\text{Bi}_2\text{O}_2\text{CO}_3$ could be efficient to degrade some refractory pollutants in the aqueous environment.

In this study, p–n heterojunction photocatalyst with unique structure was synthesized by a facile hydrothermal loading of Co_3O_4 onto the lotus-leaf-like nanosheets $\text{Bi}_2\text{O}_2\text{CO}_3$, which has never been reported before. Furthermore, there are only few studies about the photodegradation pathways of naphthalene. Owing to the unique structural features, the photocatalytic performance of as-prepared p–n heterojunction photocatalyst $\text{Co}_3\text{O}_4/\text{Bi}_2\text{O}_2\text{CO}_3$ was investigated via the photodegradation of hardly-decomposed naphthalene under visible-light irradiation. The catalytic mechanism of the p–n heterojunction photocatalyst $\text{Co}_3\text{O}_4/\text{Bi}_2\text{O}_2\text{CO}_3$ was discussed in detail. The possible degradation pathways were proposed and discussed based on the degradation products which identified by GC–MS and the frontier electron density calculation

2. Experimental section

2.1. Materials

Bismuth nitrate hydrate ($\text{Bi}(\text{NO}_3)_3 \cdot 5\text{H}_2\text{O}$), cetyl trimethyl ammonium bromide (CTAB), sodium carbonate (Na_2CO_3), cobalt(II) acetate tetrahydrate ($\text{Co}(\text{CH}_3\text{COO})_2 \cdot 4\text{H}_2\text{O}$) and other chemicals used in the experiments were of analytically pure grade (99%). These chemicals were purchased from Shanghai Chemical Reagent Ltd., without further purification. Deionized water was used throughout this study.

2.2. Preparation of $\text{Bi}_2\text{O}_2\text{CO}_3$

The lotus-leaf-like nanosheets $\text{Bi}_2\text{O}_2\text{CO}_3$ sample was synthesized by a facile hydrothermal process. $\text{Bi}(\text{NO}_3)_3$ (2 mmol) and CTAB (0.1 g) were added in 80 ml of HNO_3 (1.0 M) solution and subjected to stir for 20 min. After the mixture was fully dissolved, Na_2CO_3 (10 mmol) was added and a white precipitate formed immediately. This suspension was magnetically stirred for 30 min to complete the precipitation reaction. The suspension was then transferred into 100 ml Teflon-lined stainless-steel autoclave and heat treated at 60 °C for 24 h. Then the reactor was naturally cooled to room temperature. The obtained sample was collected and washed several times with deionized water and dried at 60 °C for overnight.

2.3. Preparation of p–n heterojunction photocatalyst $\text{Co}_3\text{O}_4/\text{Bi}_2\text{O}_2\text{CO}_3$

The p–n heterojunction photocatalyst $\text{Co}_3\text{O}_4/\text{Bi}_2\text{O}_2\text{CO}_3$ (Co_3O_4 and $\text{Bi}_2\text{O}_2\text{CO}_3$ with mass ratio of 1:6) was prepared via in-situ hydrothermal method. Tetrahydrate cobalt acetate ($\text{Co}(\text{CH}_3\text{COO})_2 \cdot 4\text{H}_2\text{O}$), 12.41 mg) was dissolved in 12 mL deionized water and 12 mL ethyl alcohol, then stirred vigorously for 30 min. The $\text{Bi}_2\text{O}_2\text{CO}_3$ powder (24 mg) was subsequently added into the above solution under ultrasonic at 80 °C for 3 h. The solution was transferred into a Teflon-lined stainless-steel autoclave and reacted at 150 °C for 3 h. The product was obtained by centrifugation and dried at 60 °C for 12 h. The other samples $\text{Co}_3\text{O}_4/\text{Bi}_2\text{O}_2\text{CO}_3$ ($\text{Bi}_2\text{O}_2\text{CO}_3$ and Co_3O_4 with a mass ratio of 1:2, 1:4, 1:8, 1:10) were also synthesized by the above procedure, and the different content of Co_3O_4 was achieved by adjusting the amount of $\text{Co}(\text{CH}_3\text{COO})_2 \cdot 4\text{H}_2\text{O}$. Briefly, the sample was denoted as Co/Bi-a, in which Co and Bi represent Co_3O_4 and $\text{Bi}_2\text{O}_2\text{CO}_3$, respectively, a represents mass ratio of $\text{Bi}_2\text{O}_2\text{CO}_3$ and Co_3O_4 . For comparison, pure Co_3O_4 nanocrystals were synthesized under the same conditions without adding $\text{Bi}_2\text{O}_2\text{CO}_3$.

2.4. Characterization

The crystallinity of the sample was determined by X-ray diffraction (XRD) at room temperature using a XRD-6000 X-ray powder diffractometer (Shimadzu) with monochromatic Cu-K radiation at a setting of 40 kV and 30 mA. The field emission scanning electron microscopy (FESEM) images were taken on a FEI-quanta 250 scanning electron microscope with an acceleration voltage of 10 kV. Transmission electron micrograph (TEM) and high-resolution transmission electron microscopy (HRTEM) were taken on a JEM-200CX instrument. X-ray photo-electron spectroscopy (XPS) was conducted to identify surface chemical composition and chemical states of the catalysts on a PHI5000 Versa Probe electron spectrometer with monochromatized Al-K radiation (ULVAC-PHI, Japan). UV–Vis absorption spectra were carried out using a Lambda 750 (PerkinElmer) spectrophotometer at a wavelength range of 200–800 nm. Fluorescence emission spectra and time-resolved fluorescence measurements were recorded over a wavelength range of 340–800 nm on a Horiba Fluorolog 3–22 type fluorescence spectrophotometer with excitation wavelength of 320 nm. The photoelectrochemical characterization was conducted on an electrochemical workstation (CHI760E, Shanghai, China) with a standard three-electrode system. The prepared samples were loaded onto ITO electrode ($1\text{ cm} \times 2\text{ cm}$ squares) and served as the working electrode. Pt plate and Ag/AgCl electrode were used as the counter and reference electrodes, respectively. The electrolyte was 0.1 M Na_2SO_4 aqueous solution. A 500 W xenon lamp was employed to provide light source. The photocurrent experiments were performed using an electrochemical station (CHI660D, Shanghai Chenhua Ltd., China) in a conventional three-electrode configuration. The electrolyte was 0.01 M Na_2SO_4 aqueous solution.

2.5. Photocatalytic reactions

The photocatalytic activities of the as-prepared samples were systematically verified by degrading naphthalene (NA, 10 mg/L) under visible-light irradiation. The simulated irradiation system (XPA-7, Nanjing, China) consisted of 500 W Xenon lamp, 400 nm cut-off filters, 50 mL quartz reaction cells, and a water cooler trough (preventing the thermal catalytic effect). In a typical experiment, the catalyst (25 mg) was dispersed into 50 mL solution containing the targeted pollutant. The initial concentration of naphthalene was 10 mg/L and acetonitrile was used as co-solvent (the volume ratio of acetonitrile and water was 1:1000). Prior to light illumination, the suspension was magnetically stirred for an hour under dark to ensure the establishment of adsorption-desorption equilibrium of naphthalene on the surface of the photocatalyst. At given time intervals of visible-light irradiation, about 3 mL of the suspension was taken from the reaction colorimetric tube,

centrifuged and filtered using a 0.22 μm Millipore filter to remove the particles. The concentration of filtrates was subsequently analyzed by the using an Agilent 1200 high performance liquid chromatography (HPLC). To verify the reproducibility of photocatalytic reactions, duplicate runs were performed under the same condition for all the reactions.

2.6. Analytic methods

The concentration of NA was accurately measured by using an Agilent 1200 high performance liquid chromatography (HPLC) with a UV detector and a C18 reversed phase column (5 μm , $4.6 \times 150\text{ mm}$). The activity of catalyst could be intuitively performed by degradation efficiency of NA through calculation. The photocatalytic degradation efficiency was calculated by the following expression:

$$\eta = \frac{C_0 - C_t}{C_0} \times 100\%$$

Where is the photocatalytic efficiency; C_0 is the concentration of reactant before illumination; C_t is the concentration of reactant after illumination of t mins. During the HPLC analysis, methanol-water (4:1, v/v) was used as the mobile phase at 1 mL/min and detection of NA was at the wavelength of 254 nm. The injection volume for each sample was 20 μL . The mediate degradation products of NA were analyzed by gas chromatography-mass spectrometer (GC–MS) equipped with a TG-5SILMS column (30 m \times 0.25 mm, 0.25 μm). Before GC–MS analysis, the aqueous sample (50 mL) was centrifuged and filtered through 0.22 μm Millipore filter to remove the particles in suspension. Then the obtained solution was extracted with a specific volume of dichloromethane (2:1, v:v) for three times. The extracted solution was concentrated to about 1 mL by rotary evaporation and dried under flowing nitrogen, then was dissolved in 1 mL n-hexane.

For the GC–MS analysis, the approach was as follows: the temperature of GC was initially 50 °C and held for 1 min, and then it increased to 160 °C at 10 °C/min, subsequently it raised up to 290 °C at a rate of 4 °C/min and held for 5 min. The injection, transmission line and ion source temperatures were 260 °C, 290 °C, and 280 °C, respectively. Helium was used as the carrier gas at 1.0 mL/min. Election impact (EI) mode was utilized and the ionizing election energy was set to 70 eV.

2.7. Theoretical calculation of NA

Gaussian 09 W program at B3LYP/6–311 + G* level with a minimum energy was used to conduct the molecular orbital calculation of NA. The frontier electron densities (FEDs) of highest occupied molecular orbital (HOMO) and the lowest unoccupied molecular orbital (LUMO) of each atom were determined based on Gaussian output files. In addition, values of ($\text{FED}_{\text{HOMO}}^2 + \text{FED}_{\text{LUMO}}^2$) were calculated to predict the possible reaction sites in the naphthalene molecule.

3. Results and discussion

3.1. Phase structure and composition

It has been considered that XRD was used to determine the phase purities and crystallographic structures. Fig. 1 shows that the diffraction peaks of the bare $\text{Bi}_2\text{O}_2\text{CO}_3$ (curve a) can be well matched to the peaks of pure tetragonal $\text{Bi}_2\text{O}_2\text{CO}_3$ (JCPDS card no. 41-1448), which at $2\theta = 12.9^\circ$, 32.7° , 46.9° , and 57.0° could be assigned to the (002), (110), (020) and (123) facets, respectively. In addition, for the Co_3O_4 (curve b), the broad diffraction peaks located at 31.3° , 36.8° , 44.8° and 65.2° correspond to the (220), (311), (400), and (440) planes of spinel type cubic Co_3O_4 (JCPDS No.74-2120). Curves c–f in Fig. 1 are the wide-angle XRD patterns of p–n heterojunction photocatalyst $\text{Co}_3\text{O}_4/\text{Bi}_2\text{O}_2\text{CO}_3$ with different Co_3O_4 amounts. It is clear that the intensity of diffraction peaks of $\text{Bi}_2\text{O}_2\text{CO}_3$ shifts to lower with the increment of

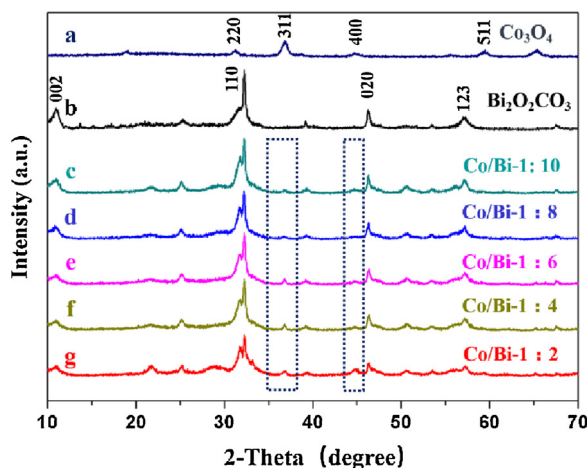


Fig. 1. XRD patterns of pure $\text{Bi}_2\text{O}_2\text{CO}_3$, Co_3O_4 and $\text{Co}_3\text{O}_4/\text{Bi}_2\text{O}_2\text{CO}_3$ composite with different mass ratio of Co_3O_4 and $\text{Bi}_2\text{O}_2\text{CO}_3$.

Co_3O_4 amounts, which can be ascribed to the overlapping of the dominant diffraction peak of these two components. Moreover, the weak diffraction peaks located at 36.8° and 44.8° , which correspond to the (311) and (400) planes of Co_3O_4 , can be found in XRD patterns (curve c–f). When increasing the content of Co_3O_4 , the intensity of the characteristic peaks indexed to Co_3O_4 also increases and becomes more obvious, which indicates that crystallinity of composites become higher. This result further demonstrates that Co_3O_4 is successfully generated on the surface of $\text{Bi}_2\text{O}_2\text{CO}_3$. Comparing to the diffraction peaks of pure Co_3O_4 and pure $\text{Bi}_2\text{O}_2\text{CO}_3$, no new crystal phases are found. It can be concluded that there are no new substances formed during the process of preparation and the crystalline phase structure of $\text{Bi}_2\text{O}_2\text{CO}_3$ is not affected by the addition of Co_3O_4 . In order to further verify the existence of Co_3O_4 , the samples were examined by XPS,

FESEM, and TEM analysis.

To determine the surface chemical composition and valence state of various species, the sample of pure $\text{Bi}_2\text{O}_2\text{CO}_3$, Co_3O_4 , and $\text{Co}/\text{Bi}-1:6$ were measured by XPS. Figure S1 shows the XPS survey scan spectra of samples. As expected, the XPS spectrum of $\text{Co}/\text{Bi}-1:6$ contains Bi, C, O and Co elements, which consistent with the chemical composite of the photocatalyst. The high-resolution XPS spectra of Bi 4f, O 1s, C 1s, Co 2p were shown in Fig. 2(a–d), respectively. As for the high-resolution Co 2p XPS spectrum of Co_3O_4 (Fig. 2a), two peaks at 780.5 and 796 eV are associated with Co 2p_{1/2} and Co 2p_{3/2}, respectively. It is clear that the observed Co 2p peaks of $\text{Co}/\text{Bi}-1:6$ shifted to lower binding energies. A similar result was also observed for the binding energies of Bi 4f, C 1s and O 1s for the sample $\text{Bi}_2\text{O}_2\text{CO}_3$ in Fig. 2(b–d). The binding characteristic orbital energies of Bi 4f_{7/2} and Bi 4f_{5/2} are observed with peaks located at 159.2 and 164.5 eV, respectively, indicating the main chemical state of Bi in the sample is +3 [42]. It is obvious that the peak position of Bi has a 0.2 eV shift to the higher energy compared with the composite $\text{Co}/\text{Bi}-1:6$, which may be attributed to the heterostructure effect between $\text{Bi}_2\text{O}_2\text{CO}_3$ and Co_3O_4 [43]. Fig. 2c shows the high-resolution C 1s spectrum, which can be fitted with two peaks. In the $\text{Bi}_2\text{O}_2\text{CO}_3$ sample, the peak located at 284.5 eV is usually assigned to adventitious carbon and another weak peak positioned at 288.4 eV is corresponded to carbonate ion in $\text{Bi}_2\text{O}_2\text{CO}_3$ [42]. The C 1s' peaks in $\text{Co}/\text{Bi}-1:6$ were also shifted down by 0.3 eV. O 1s peaks of $\text{Co}/\text{Bi}-1:6$ illustrated in Fig. 2d can be deconvoluted into three peaks at 529.7, 531.5 and 532.2 eV, which correspond to the Bi–O bonds in $[\text{Bi}_2\text{O}_2]$ slabs or Co–O bonds [44,45], –OH bonds of the surface adsorbed water [46] and carbonate species [47], respectively. It is proposed that on the sample surface there are many adsorption oxygen atoms existed, which could become captives of photogenerated electron-hole pairs directly or indirectly, and further inhibit the photogenerated electron-hole recombination to increase the quantum efficiency, and hence the photocatalytic activity of the sample would be effectively improved. The result also clearly indicates the presence of Co_3O_4 , implying the

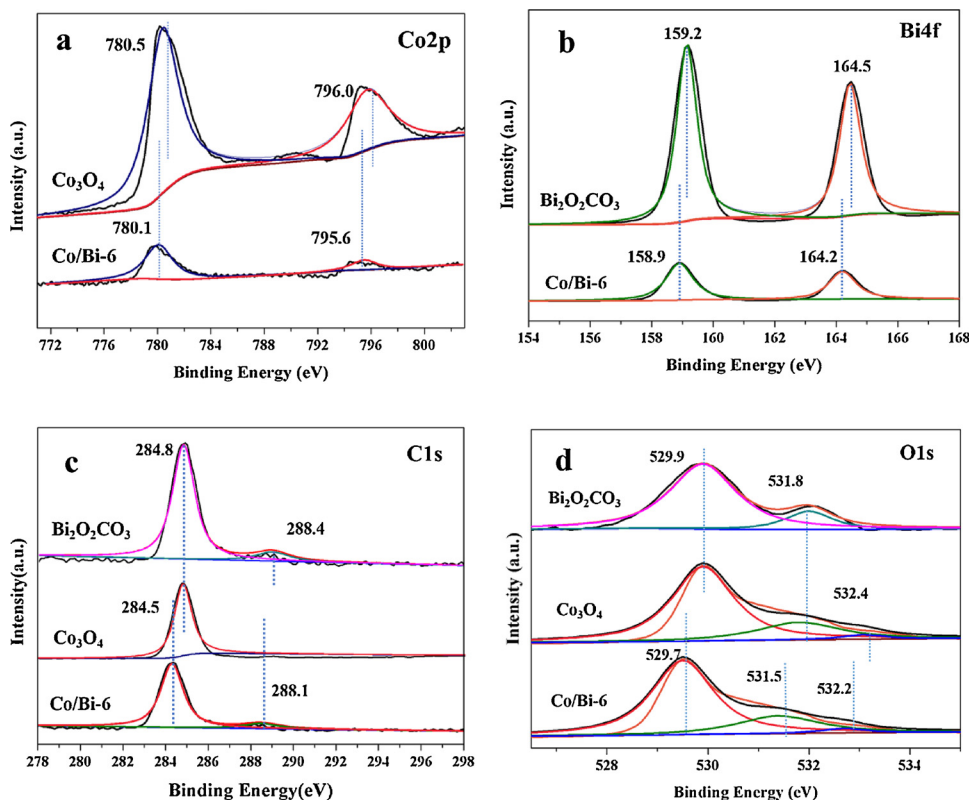


Fig. 2. XPS spectra of as-prepared $\text{Bi}_2\text{O}_2\text{CO}_3$, Co_3O_4 and $\text{Co}_3\text{O}_4/\text{Bi}_2\text{O}_2\text{CO}_3$. a: Co 2p; b: Bi 4f; c: C 1s and d: O 1s.

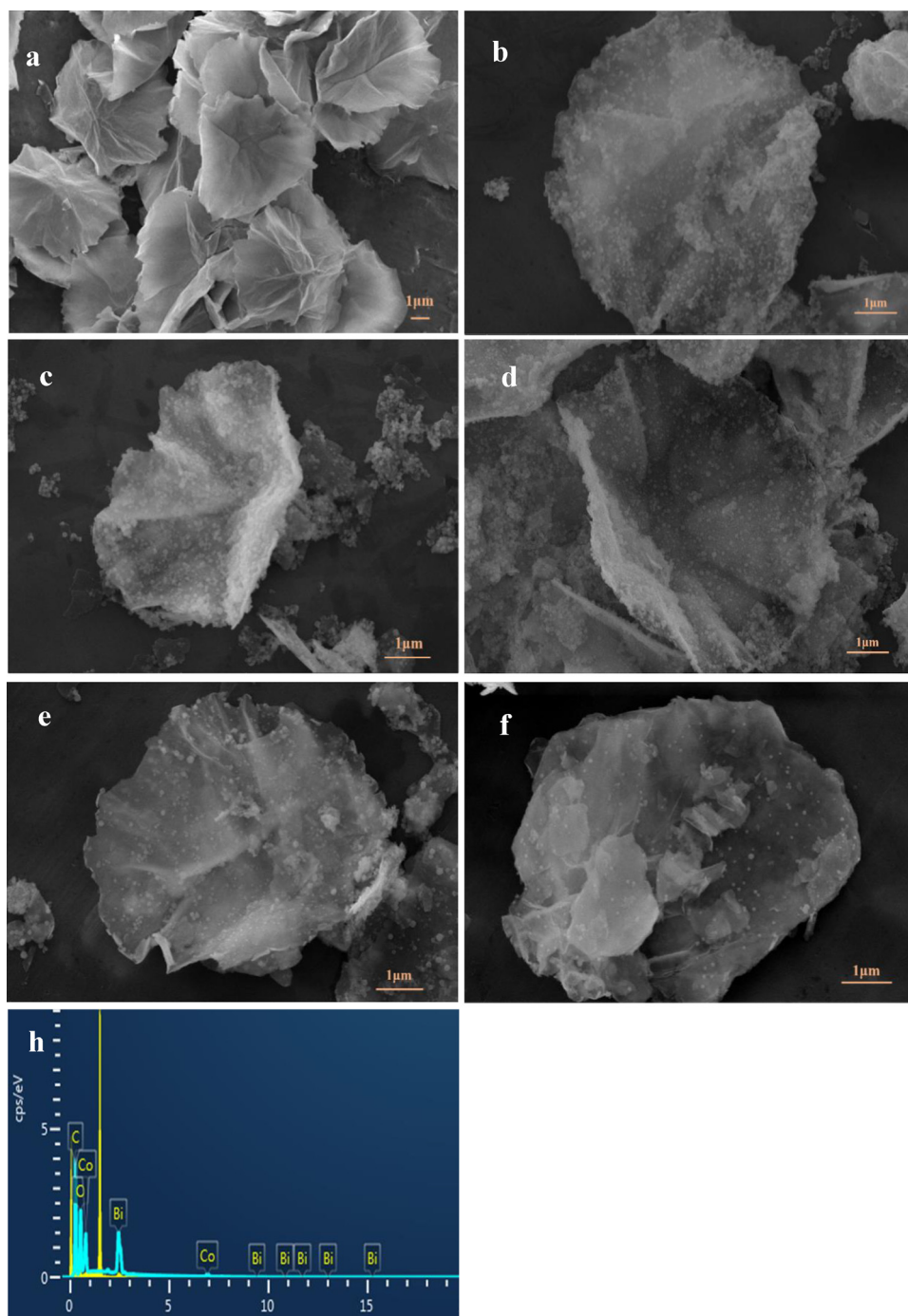


Fig. 3. a–f: the SEM images of $\text{Bi}_2\text{O}_2\text{CO}_3$, Co/Bi-1:2, Co/Bi-1:4, Co/Bi-1:6, Co/Bi-1:8 and Co/Bi-1:10, h: EDS pattern of Co/Bi-1:6.

formation of $\text{Co}_3\text{O}_4/\text{Bi}_2\text{O}_2\text{CO}_3$ heterojunctions.

3.2. Morphology and crystal structure

The morphologies of the as-prepared photocatalyst were investigated by FESEM, which further demonstrates the successful preparation of composite $\text{Co}_3\text{O}_4/\text{Bi}_2\text{O}_2\text{CO}_3$. As depicted in Fig. 3a, the local photograph of $\text{Bi}_2\text{O}_2\text{CO}_3$ represents regular lotus-leaf-like flakes which consist of the thin nanosheets ($< 2 \text{ nm}$) piling together. The $\text{Co}_3\text{O}_4/\text{Bi}_2\text{O}_2\text{CO}_3$ heterogeneous catalysts with different loading amounts of Co_3O_4 are displayed in Fig. 3(b–f). It is obvious that the morphology and microstructure of pure $\text{Bi}_2\text{O}_2\text{CO}_3$ have not been destroyed or changed after hybrid with Co_3O_4 . Seen from the high-magnification

images of $\text{Co}_3\text{O}_4/\text{Bi}_2\text{O}_2\text{CO}_3$, as the increasing loading amount of Co_3O_4 nanocrystals, the number of cube Co_3O_4 nanoparticles formed on the surface of $\text{Bi}_2\text{O}_2\text{CO}_3$ grows. When the ratio of $\text{Co}_3\text{O}_4/\text{Bi}_2\text{O}_2\text{CO}_3$ is greater than 1:6, the agglomeration of Co_3O_4 could happen, which may cover the surface active sites of $\text{Bi}_2\text{O}_2\text{CO}_3$, thus would not be conducive to improve the degradation efficiency. The results are consistent with that in the photocatalytic experiments.

While surface morphology can be observed by SEM, the detailed microstructures of the samples need to be examined by TEM and HRTEM. Fig. 4a and b provide the overview of $\text{Bi}_2\text{O}_2\text{CO}_3$ and Co_3O_4 , respectively. The images of $\text{Bi}_2\text{O}_2\text{CO}_3$ show that the pure $\text{Bi}_2\text{O}_2\text{CO}_3$ flakes are thin and are formed by a cluster of slices together, so that the edge of the nanosheets is almost transparent, the shape of which looks

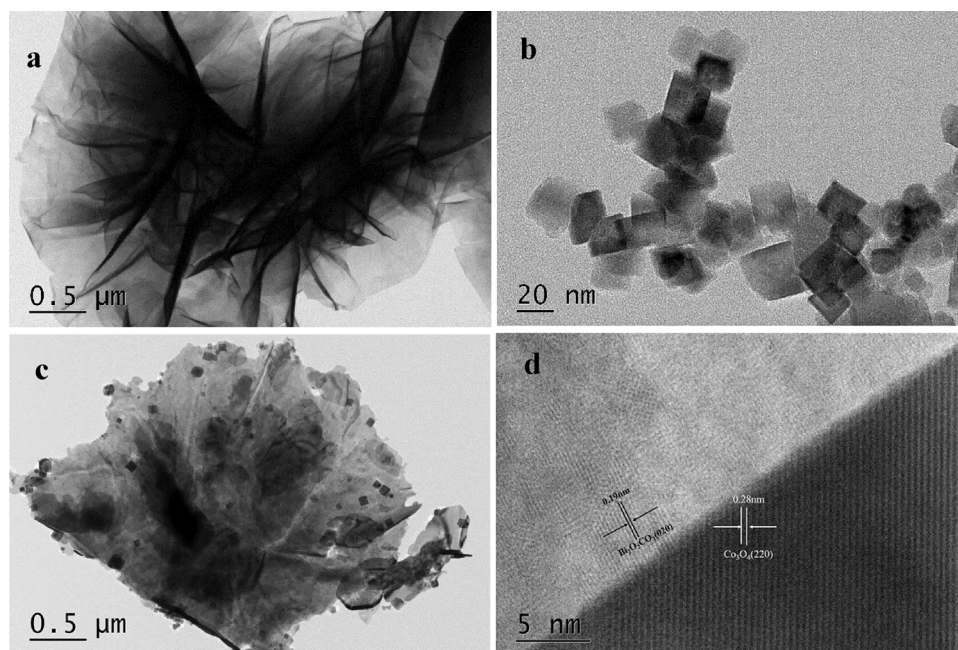


Fig. 4. TEM images of a: $\text{Bi}_2\text{O}_2\text{CO}_3$, b: Co_3O_4 , c: Co/Bi-1:6, d: HRTEM image of Co/Bi-1:6.

like the lotus leaf. The morphology of Co_3O_4 by hydrothermal process looks like cube-sugar nanocrystals with an average size of approximately 20–40 nm in Fig. 4b. The addition of Co_3O_4 does not significantly change the size of nanoparticles itself and the shape of the prepared $\text{Bi}_2\text{O}_2\text{CO}_3$ in the sample of Co/Bi-1:6 (Fig. 4c). Moreover, it can be seen that the Co_3O_4 nanocrystals are assembled on the surfaces of the $\text{Bi}_2\text{O}_2\text{CO}_3$ nanosheets with uniform distribution, coinciding with the conclusion from SEM observation. Fig. 4d is a typical HRTEM image of Co/Bi-1:6 heterogeneous nanostructure. There are two different crystal structures with the interplanar spacing of ca 0.19 nm and 0.28 nm, which correspond to the (020) planes of tetragonal $\text{Bi}_2\text{O}_2\text{CO}_3$ [48] and (220) planes of cubic Co_3O_4 [38], respectively. The results proved the formation of the heterojunction between $\text{Bi}_2\text{O}_2\text{CO}_3$ and Co_3O_4 .

Fig. 5a and b depict FESEM-EDS elemental mapping of $\text{Bi}_2\text{O}_2\text{CO}_3$ and Co/Bi-1:6, respectively. All the elements from the prepared materials are distributed uniformly in the images. The elemental mapping of $\text{Bi}_2\text{O}_2\text{CO}_3$ sample disclosed in Fig. 5a demonstrates the distribution of Bi, C, and O elements throughout the $\text{Bi}_2\text{O}_2\text{CO}_3$ sample. Besides these elements, for Co/Bi-1:6, the element of Co is observed (Fig. 5b). Furthermore, EDS analysis (Fig. 3h) certifies the elemental composition of Co/Bi-1:6, which also reveals the coexistence of Bi, C, O, and Co elements. Based on the above characterization results, the successful synthesis of $\text{Co}_3\text{O}_4/\text{Bi}_2\text{O}_2\text{CO}_3$ can be confirmed sufficiently.

3.3. Optical property analyses

The samples were analyzed by UV–vis diffuse reflectance spectroscopy (DRS) to investigate the changes in optical properties caused by the loaded Co_3O_4 . UV–vis absorption spectra of $\text{Bi}_2\text{O}_2\text{CO}_3$, Co_3O_4 , $\text{Co}_3\text{O}_4/\text{Bi}_2\text{O}_2\text{CO}_3$ are displayed in Fig. 6a. It can be clearly seen that bare Co_3O_4 nanocrystals show distinct adsorption both in the ultraviolet and visible regions. Moreover, the intensity of absorbance of the composite increases significantly in the range of 200–800 nm compared with $\text{Bi}_2\text{O}_2\text{CO}_3$, which indicates that the band edge of absorption of $\text{Co}_3\text{O}_4/\text{Bi}_2\text{O}_2\text{CO}_3$ has been broadened to the visible light region, thus should possess better visible-light photocatalytic performance than that of pure $\text{Bi}_2\text{O}_2\text{CO}_3$. The adsorption edge indicates that the visible light adsorption relevant to the band gap is not because of the impurity level but is due to the intrinsic transition of these semiconductor [49]. For

crystalline semiconductor of $\text{Bi}_2\text{O}_2\text{CO}_3$ and Co_3O_4 , the band gap energy (E_g) was calculated by the following formula (1):

$$\alpha h\nu = A(h\nu - E_g)^n \quad (1)$$

Where α , h , ν , E_g and A are the absorption coefficient, Planck's constant, light frequency, band gap and a constant, respectively. The index n depends on the electronic transition of the semiconductor, $n = 2$ for direct-gap semiconductor and $n = 0.5$ for an indirect-gap semiconductor. For $\text{Bi}_2\text{O}_2\text{CO}_3$ and Co_3O_4 , n is 0.5 [50,51]. Fig. S2(a–g) shows the Kubelka–Munk transformed reflectance spectra of pure $\text{Bi}_2\text{O}_2\text{CO}_3$, Co_3O_4 , Co/Bi-1:2, Co/Bi-1:4, Co/Bi-1:6, Co/Bi-1:8 and Co/Bi-1:10, where the band gap energy can be estimated from the intercept of the tangent to the plot of $(\alpha h\nu)^2$ vs. radiation energy ($h\nu$). The obtained band gap energy for pure Co_3O_4 and $\text{Bi}_2\text{O}_2\text{CO}_3$ are 2.13 eV and 2.98 eV. As for the composite $\text{Co}_3\text{O}_4/\text{Bi}_2\text{O}_2\text{CO}_3$ materials, the values of band gap energy are 2.33 eV, 2.38 eV, 2.41 eV, 2.42 eV and 2.54 eV for Co/Bi-1:2, Co/Bi-1:4, Co/Bi-1:6, Co/Bi-1:8 and Co/Bi-1:10, respectively. It significantly indicates that the calculated band gap energies of composite $\text{Co}_3\text{O}_4/\text{Bi}_2\text{O}_2\text{CO}_3$ are lower than that of pure $\text{Bi}_2\text{O}_2\text{CO}_3$, which means that $\text{Co}_3\text{O}_4/\text{Bi}_2\text{O}_2\text{CO}_3$ heterogeneous semiconductor could generate more electron-hole pairs under visible light excitation [14].

The photoluminescence (PL) emission spectra are widely used to disclose the efficiency of photo-induced electrons and holes in trapping, immigration and transfer, meanwhile to investigate the fate of charge carrier in semiconductor particles. Photocatalysts generate electrons and holes after being activated by the light. During the process, recombination of some electrons and holes can release energy in the form of fluorescence emission, which manifests that the decrease in the recombination rate gives rise to a low PL intensity [29]. The fluorescence emission spectra of the samples excited at a wavelength 365 nm. As revealed in the Fig. 6b, the intensity of pure $\text{Bi}_2\text{O}_2\text{CO}_3$ powders is relatively low, indicating that electrons and holes of $\text{Bi}_2\text{O}_2\text{CO}_3$ are easily recombined. After $\text{Bi}_2\text{O}_2\text{CO}_3$ and Co_3O_4 combined, the intensity of the PL peak for Co/Bi-1:6 heterojunction photocatalyst decreases, which should be attributed to the addition of Co_3O_4 . The PL results confirm that the formation of heterojunctions has a positive effect to hinder the recombination of electrons and holes.

To gain further insight into the charge carrier transfer dynamic

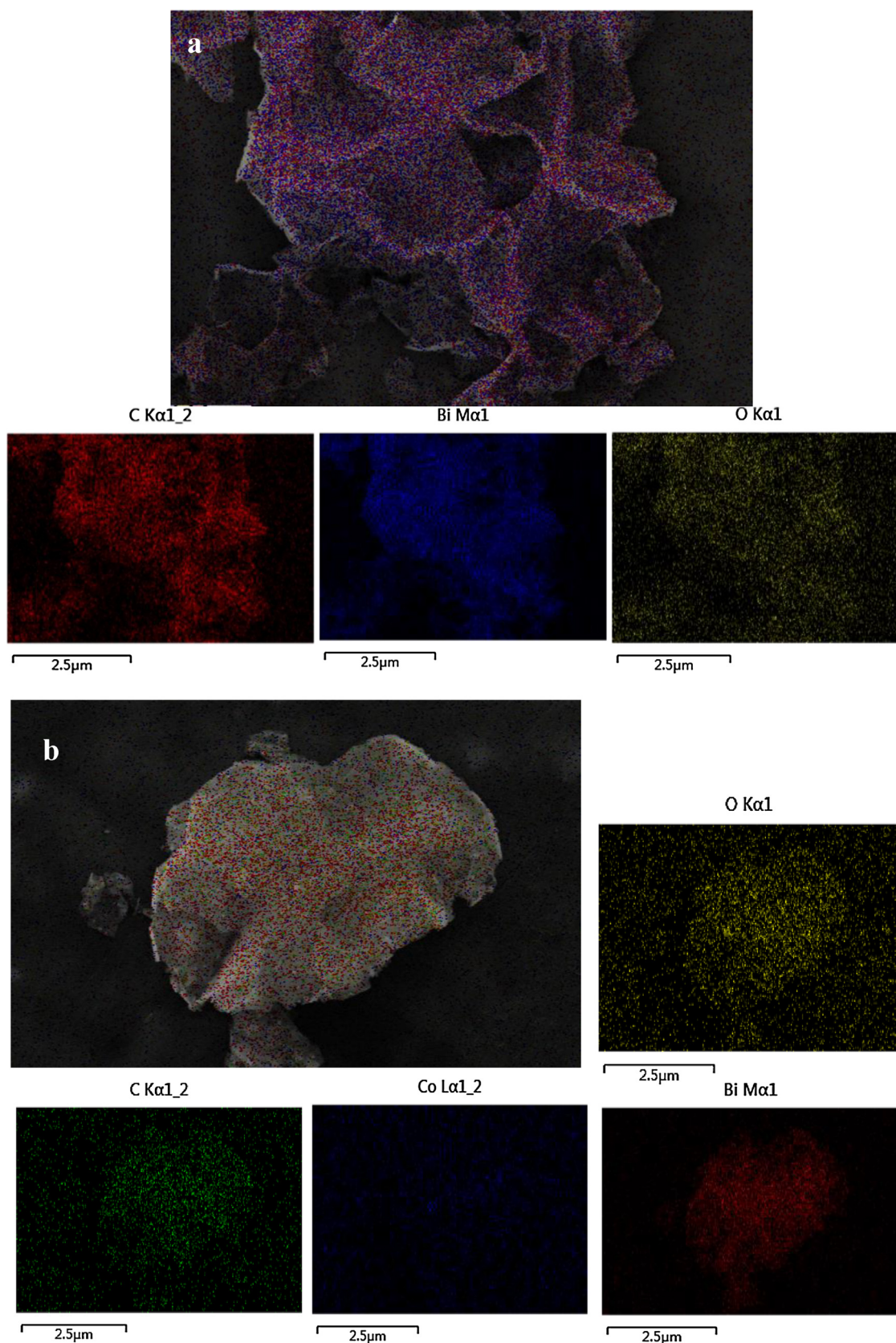


Fig. 5. FESEM-EDS element mapping of a: $\text{Bi}_2\text{O}_2\text{CO}_3$ and b: Co/Bi-1:6 .

processes, $\text{Bi}_2\text{O}_2\text{CO}_3$ and Co/Bi-1:6 are obtained in Fig. 6c. To quantitatively analyze the PL lifetime based on the time-resolved fluorescence decay measurement, the exponential functions to fit the curves were

applied, which correspond to the Eq. (2):

$$f(t) = B + A_1 \times \exp(-t/\tau_1) + A_2 \times \exp(-t/\tau_2) \quad (2)$$

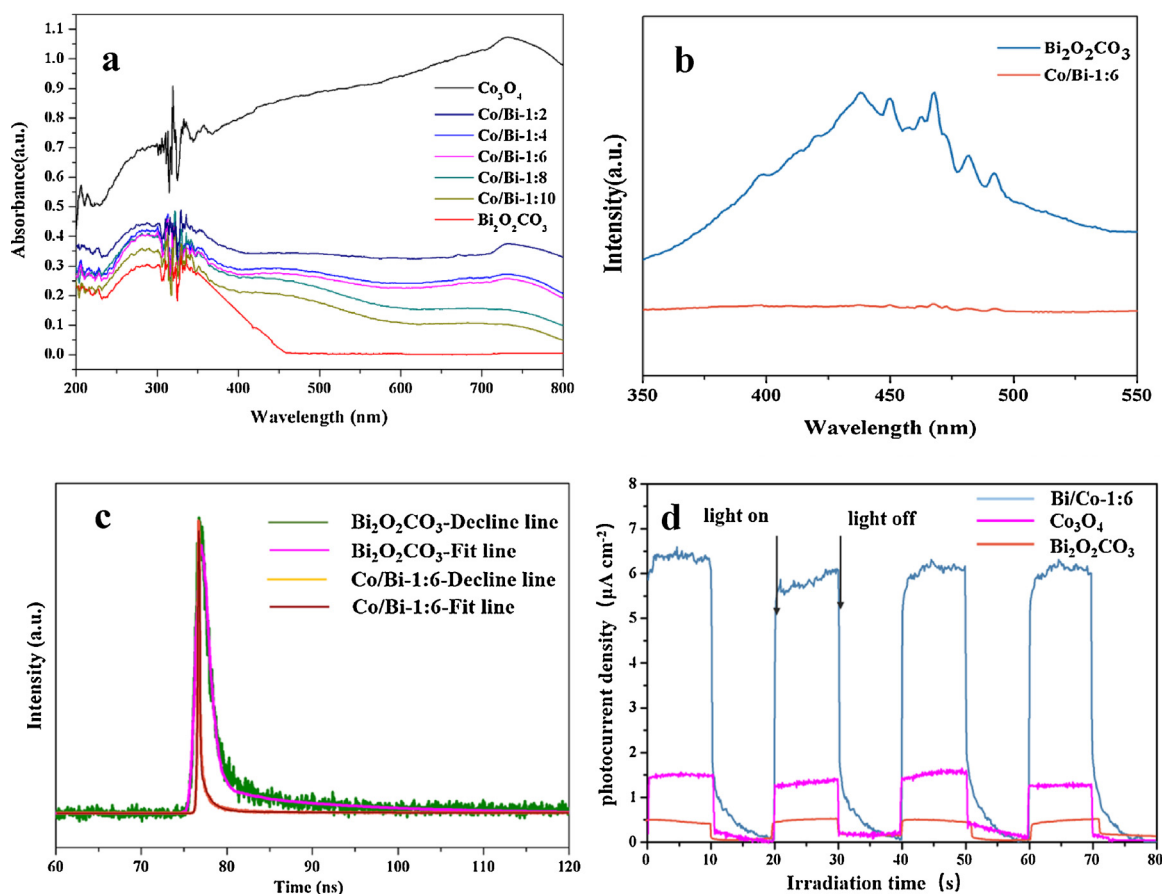


Fig. 6. a: UV-vis absorption spectra of the samples: $\text{Bi}_2\text{O}_2\text{CO}_3$, Co_3O_4 , $\text{Co}_3\text{O}_4/\text{Bi}_2\text{O}_2\text{CO}_3$, b: fluorescence emission spectra of different samples $\text{Bi}_2\text{O}_2\text{CO}_3$ and Co/Bi-1:6 , c: time-resolved fluorescence decay of the corresponding samples $\text{Bi}_2\text{O}_2\text{CO}_3$ and Co/Bi-1:6 followed 365 nm laser excitation, d: Photocurrents of pure $\text{Bi}_2\text{O}_2\text{CO}_3$, Co_3O_4 and Co/Bi-1:6 electrodes under visible light irradiation.

Table 1

Summary of time-resolved fluorescence decay data of the corresponding samples.

Samples	$\tau_1(\text{ns})$	A_1	$\tau_2(\text{ns})$	A_2	$\tau_{\text{avg}}(\text{ns})$
$\text{Bi}_2\text{O}_2\text{CO}_3$	0.157	0.013	3.650	0.00287	0.169
Co/Bi-1:6	0.358	0.158	15.114	0.00230	0.570

Table 1 summarizes the data of the samples: the lifetimes (τ_1 and τ_2), pre-exponential factors (A_1 and A_2), and average lifetime τ_{avg} . Specifically, the average decay lifetime of charge carriers in the composite Co/Bi-1:6 is 0.570 ns, which is 3.37 times slower than that of pure $\text{Bi}_2\text{O}_2\text{CO}_3$ (0.169 ns). The prolonged decay lifetime illustrates that by coupling with Co_3O_4 photocatalysts, the recombination of electrons and holes could be effectively suppressed and a high separation of charge carriers could exist. In the photocatalytic reaction, the high separation efficiency will raise the probability of their participation before recombination, which remarkably enhances the photocatalytic efficiency [52].

Photocurrent measurement can also provide the evidence for the separation rate of the photo-generated carrier in heterojunctions. The value of photocurrent indirectly reflects the semiconductor's ability of charge carrier transfer under irradiation [53]. Fig. 6d illustrates that both the photocurrent and dark current for $\text{Bi}_2\text{O}_2\text{CO}_3$, Co_3O_4 and Co/Bi-1:6 photocatalysts under the chopped irradiation of a Xe lamp ($\lambda > 420 \text{ nm}$). The composite Co/Bi-1:6 performs the maximum photocurrent density, which is nearly 5.5 times higher than those of pristine Co_3O_4 and $\text{Bi}_2\text{O}_2\text{CO}_3$. It is well-known that the higher the value of photocurrent response is, the higher the separation rate of photo-

generated electrons-hole pairs is [32]. Based on these analyses, the formation of heterojunction with the cooperation of Co_3O_4 and $\text{Bi}_2\text{O}_2\text{CO}_3$ would be beneficial to the separation of charge carriers.

Fig. S2h depicts the electrochemical impedance spectroscopy (EIS) Nyquist plots of $\text{Bi}_2\text{O}_2\text{CO}_3$, Co_3O_4 , and Co/Bi-1:6 to investigate the interface charge separation efficiency. The radius of the arc on the EIS spectra reflects the reaction rate occurring at the surface of the electrode. The smaller diameter of Nyquist circle, the lower resistance generates, which can speed up the transfer process of surface charge [54]. Therefore, the smaller arc radius on the EIS Nyquist plot of Co/Bi-1:6 under visible light indicates that a more effective separation of photogenerated electron-hole pairs and a faster interfacial charge transfer happened, and also indirectly demonstrates that Co_3O_4 plays a key role in improving the separation efficiency of charge carriers.

Hence, the above conclusion of PL spectra, ns-level time-resolved fluorescence decay spectra, photocurrent measurement and EIS spectra undoubtedly disclose that the successful preparation of $\text{Co}_3\text{O}_4/\text{Bi}_2\text{O}_2\text{CO}_3$ heterojunction brings the benefit of comparatively low electron-hole recombination rate and a relatively higher charge separation efficiency under irradiation, and accordingly enhances the photocatalytic activity during the reaction.

3.4. Photocatalytic properties

The photocatalytic activity and chemical stability of $\text{Co}_3\text{O}_4/\text{Bi}_2\text{O}_2\text{CO}_3$ heterojunction photocatalysts with different Co_3O_4 content were evaluated in terms of photodegradation of naphthalene (NA) under visible-light irradiation (Fig. 7(a-c)). A dark adsorption experiment was carried out for 60 min prior to the visible-light irradiation to

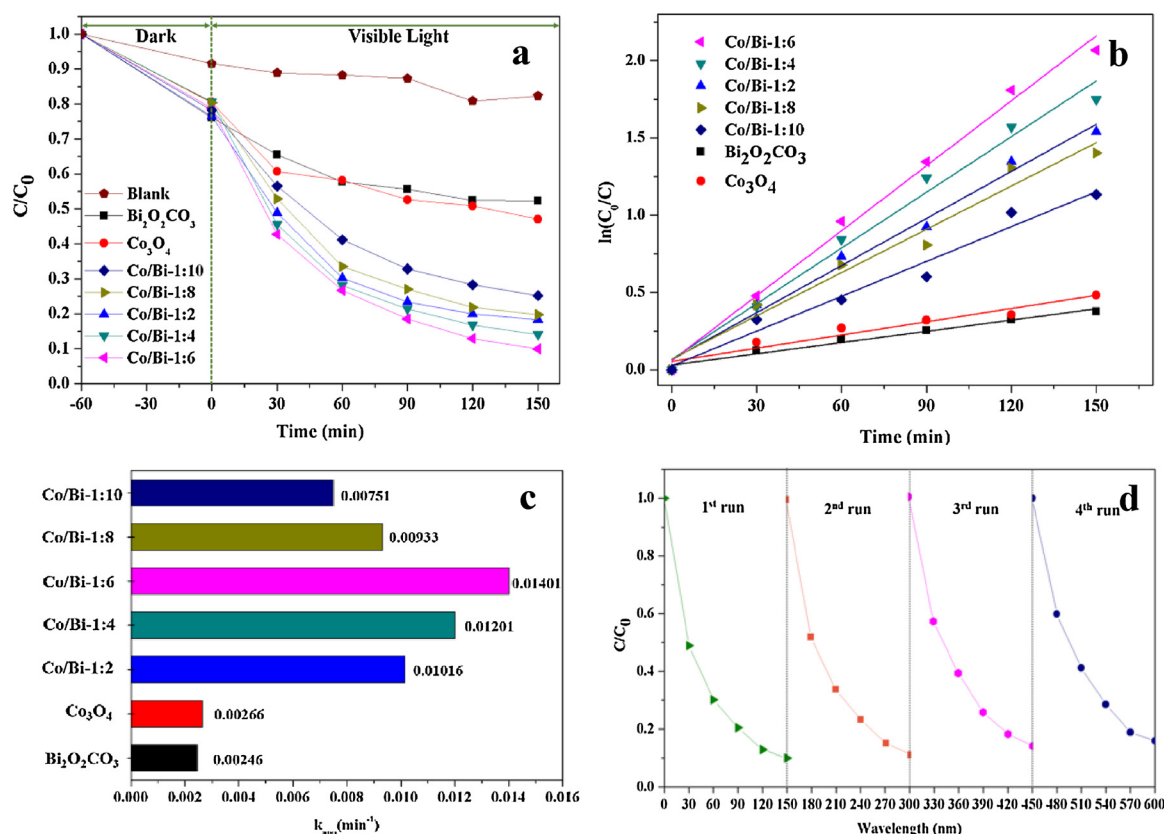


Fig. 7. a: Photocatalytic degradation, b: pseudo-first-order kinetics curves and c: k_{app} of NA (10 ppm) with adding different as-prepared photocatalysts under visible-light irradiation, d: 4 recycling runs of Co/Bi-1:6 for NA photodegradation.

achieve an equilibrium adsorption state (Fig. 7a). Moreover, photodegradation of NA without photocatalyst as a control test demonstrated that the self-degradation of NA under visible-light could almost be neglected. For comparison, the pure $\text{Bi}_2\text{O}_2\text{CO}_3$ and Co_3O_4 were also tested under the same conditions, which degraded 47.73% and 52.94% NA within 150 min. It is distinct that p-n heterojunction $\text{Co}_3\text{O}_4/\text{Bi}_2\text{O}_2\text{CO}_3$ displayed higher photocatalytic efficiency than that of bare $\text{Bi}_2\text{O}_2\text{CO}_3$ and Co_3O_4 . Specifically, with the growth of Co_3O_4 content, the photocatalytic activity of $\text{Co}_3\text{O}_4/\text{Bi}_2\text{O}_2\text{CO}_3$ exhibits a climb, after which it drops. The sample Co/Bi-1:6 shows the highest photocatalytic activity with the degradation efficiency of about 91.02%. When the mass ratio of $\text{Bi}_2\text{O}_2\text{CO}_3$ and Co_3O_4 exceeds 1:6, the degradation activity of the composite declines, indicating that the optimum mass ratio of $\text{Bi}_2\text{O}_2\text{CO}_3$ and Co_3O_4 is 1:6. Obviously, the presence of Co_3O_4 formed the p-n heterojunction with $\text{Bi}_2\text{O}_2\text{CO}_3$ has a significant influence on the photocatalytic activity. Either too much or too little of the content of Co_3O_4 is not unfavorable to improve the photodegradation efficiency. It concludes that with the increase of the Co_3O_4 amount up to the optimum ratio 1:6, the trapping sites of carriers rise, which prolongs the lifetime of charge carriers. While the formation of p-n heterojunction also facilitates to improve the photocatalytic performance. However, the amount of Co_3O_4 which exceeds the optimum content of depositing may be to the disadvantage of photodegradation activity, because excessive Co_3O_4 may incline to cluster on the $\text{Bi}_2\text{O}_2\text{CO}_3$ and does not effectively form the p-n heterojunction, which is verified by the SEM result (Fig. 3c and d). Meanwhile, too much amount of Co_3O_4 over optimum point covers more active sites on the composite surface and blocks the photogenerated electron transfer.

According to the Langmuir-Hinshelwood model, the photocatalytic degradation of NA follows pseudo-first-order reaction. The kinetic curves and their reaction rate constants for NA photodegradation over $\text{Co}_3\text{O}_4/\text{Bi}_2\text{O}_2\text{CO}_3$ are plotted and displayed in Fig. 7b, which could be

obtained from Eq. (3)

$$\ln(C_0/C) = k_{app}t \quad (3)$$

where k_{app} is the apparent reaction rate constant, C_0 and C are the initial and instantaneous concentrations of NA, respectively [55]. Based on the value of k_{app} , the photocatalytic performance of different photocatalysts can easily be compared. From the Fig. 7c, it is clear that Co/Bi-1:6 has the highest value of k_{app} (0.01401 min^{-1}), which is nearly 5.7 times larger than that of the bare $\text{Bi}_2\text{O}_2\text{CO}_3$ (0.00246 min^{-1}). In all of the as-prepared photocatalysts, the order of the photocatalytic performance is $\text{Co/Bi-1:6} > \text{Co/Bi-1:4} > \text{Co/Bi-1:2} > \text{Co/Bi-1:8} > \text{Co/Bi-1:10} > \text{Co}_3\text{O}_4 > \text{Bi}_2\text{O}_2\text{CO}_3$. The result indicates that the amount of loaded Co_3O_4 plays a key role in enhancing the photodegradation activity of the composite.

To observe the stability and reusability of the $\text{Co}_3\text{O}_4/\text{Bi}_2\text{O}_2\text{CO}_3$ samples as visible-light photocatalysts, which are crucial factors in the practice application, we repeated the photocatalytic degradation of NA by using the catalyst Co/Bi-1:6 four times and the corresponding data are represented in Fig. 7d. $\text{Co}_3\text{O}_4/\text{Bi}_2\text{O}_2\text{CO}_3$ can keep a stable and efficient photocatalytic performance after the fourth-cycle test, and only a slight loss occurs compared with the first-cycle result, which may be caused by the incomplete collection of the photocatalyst during each cycle test. The consequence shows that the photocatalysts $\text{Co}_3\text{O}_4/\text{Bi}_2\text{O}_2\text{CO}_3$ behave favorable stability and recyclability.

3.5. Photocatalytic mechanism

During the process of photocatalytic oxidation, a series of reactive species, such as holes (h^+), hydroxyl radicals ($\cdot\text{OH}$) or superoxide radicals ($\cdot\text{O}_2^-$), are supposed to be involved. To investigate the higher photocatalytic activity of the p-n heterojunction $\text{Co}_3\text{O}_4/\text{Bi}_2\text{O}_2\text{CO}_3$ relative to the pure $\text{Bi}_2\text{O}_2\text{CO}_3$ and Co_3O_4 , the reactive species trapping

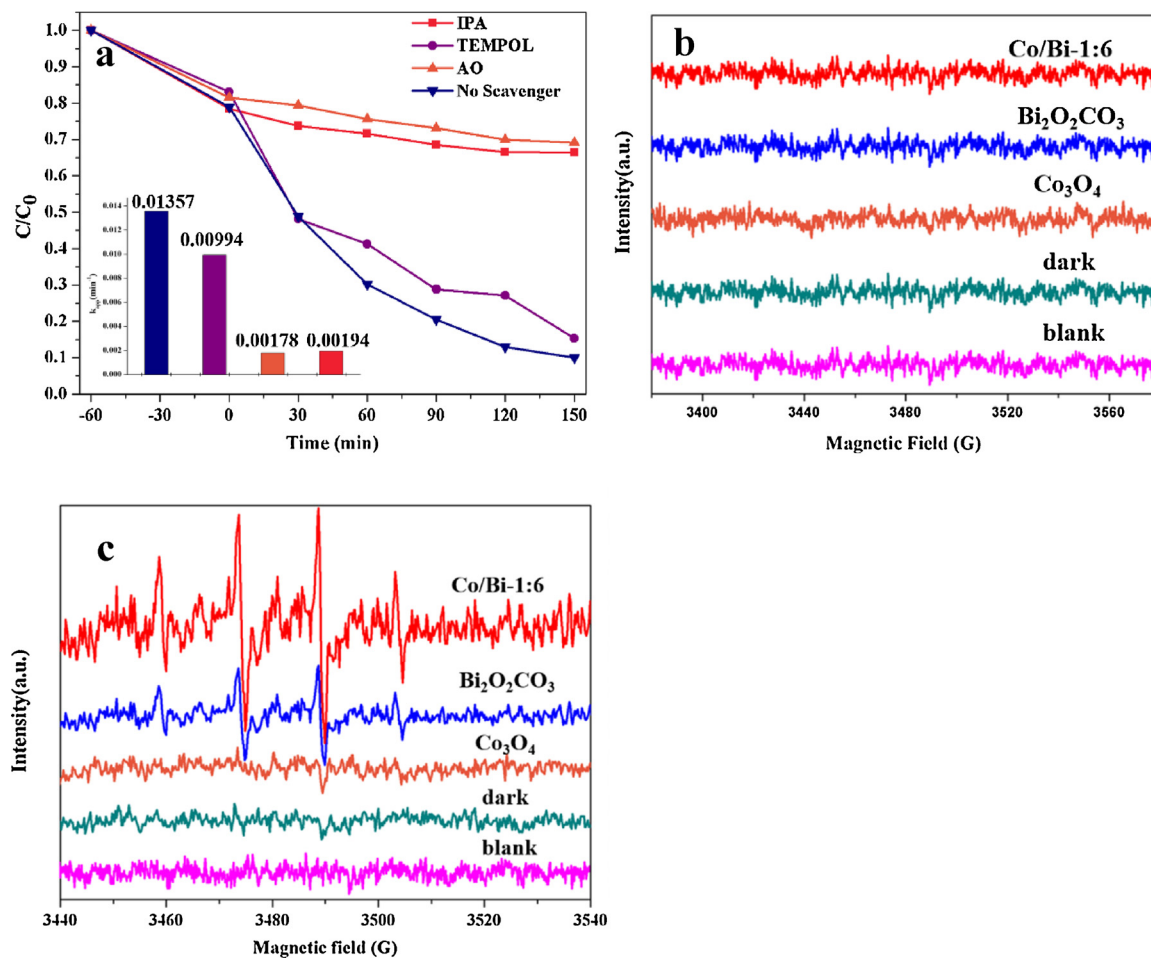


Fig. 8. a: photocatalytic activity of Co/Bi-1:6 for NA with different scavengers under visible light irradiation, b-c: DMPO spin-trapping EPR spectra of Co/Bi-1:6, pure $Bi_2O_2CO_3$ and Co_3O_4 in b: methanol dispersion and c: aqueous dispersion under visible-light irradiation.

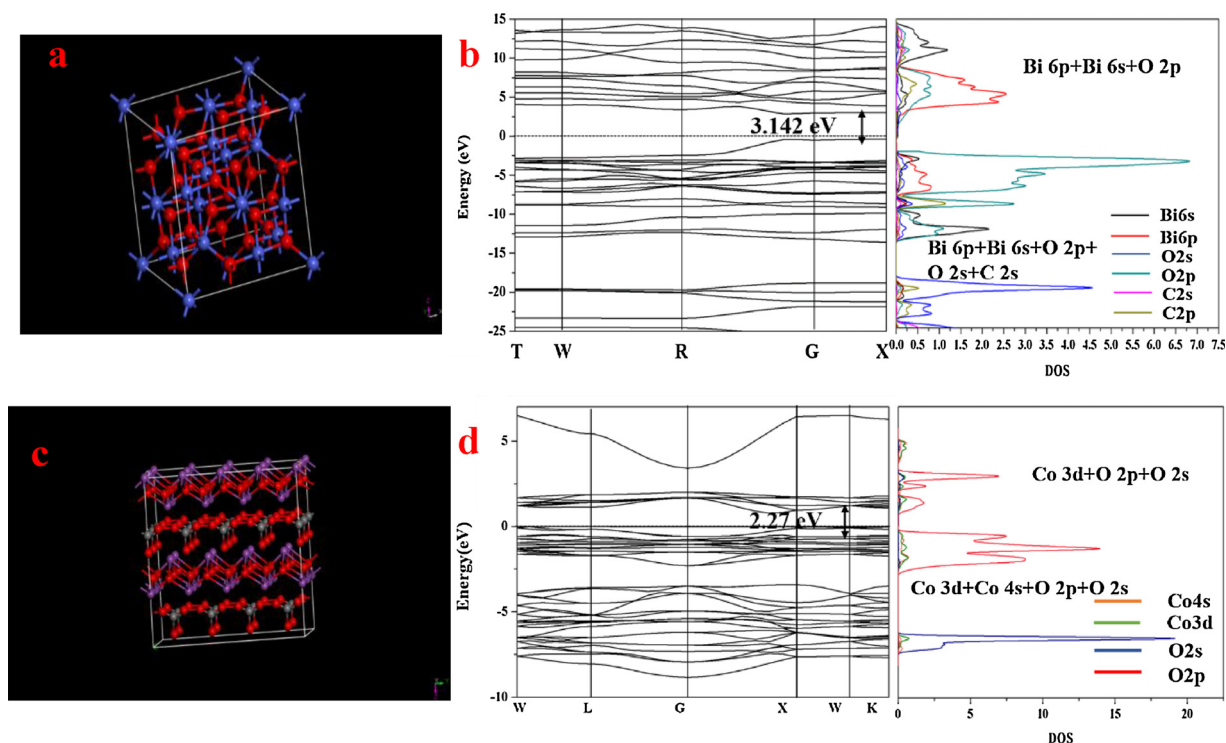


Fig. 9. Crystal structures, calculated band structures and density of states (DOS) of $Bi_2O_2CO_3$ (a, b) and Co_3O_4 (c, d).

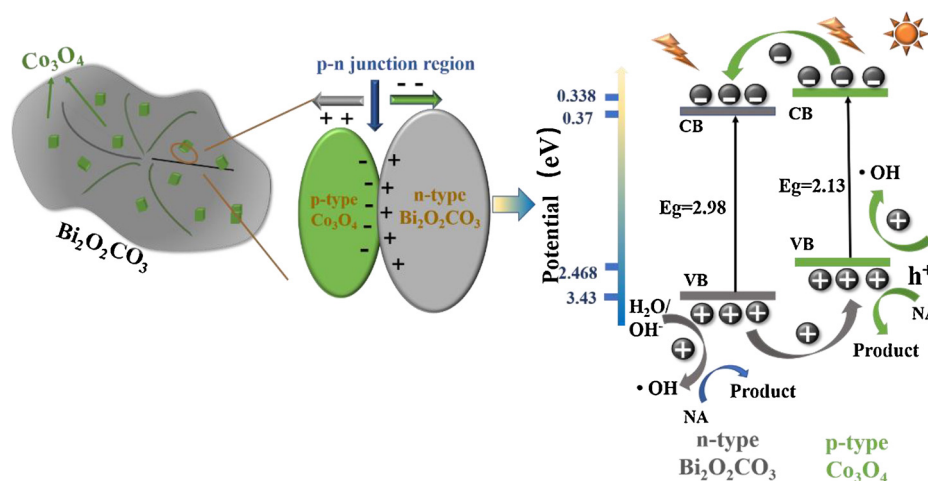


Fig. 10. The p-n heterojunction photocatalyst formation model and the photocatalytic degradation mechanism of p-n heterojunction photocatalyst $\text{Co}_3\text{O}_4/\text{Bi}_2\text{O}_2\text{CO}_3$.

experiment was conducted. In this study, isopropanol (IPA), 4-hydroxy-2, 2, 6, 6-tetramethylpiperidinyloxy (TEMPOL) and ammonium oxalate (AO) acted as the scavengers for $\cdot\text{OH}$, $\cdot\text{O}_2^-$ and h^+ were introduced into the photocatalytic process, respectively [56,57]. As a result of quenching, the photocatalytic oxidation will be partly suppressed, meanwhile, the value of k_{app} will decrease. The lower the photocatalytic activity of photocatalysts with the addition of scavengers, the more important the role of the corresponding reactive species plays in the photodegradation process. Fig. 8a displays the photocatalytic activity of $\text{Co}_3\text{O}_4/\text{Bi}_2\text{O}_2\text{CO}_3$ on the degradation of NA in the presence of different scavengers. The comparative test with no quencher was also conducted under the equal condition. As is clear from the picture, the addition of $\cdot\text{O}_2^-$ quencher did not affect the photodegradation activity of NA over Co/Bi-1:6. On the contrary, the photocatalytic efficiency was suppressed in different degrees after introducing the IPA and AO.

The characterization of electron paramagnetic resonance (EPR) was performed to further confirm the obtained results of the scavenger experiments. The tests under the dark condition and without the photocatalysts were conducted as the control group to demonstrate that no characteristic peaks were detected in all samples. No obvious characteristic peaks of $\cdot\text{O}_2^-$ were evaluated in Fig. 8b. However, the characteristic peaks of $\cdot\text{OH}$ species were detected in the sample of $\text{Bi}_2\text{O}_2\text{CO}_3$ and Co/Bi-1:6 (Fig. 6c). It is clearly seen that the signal intensity of $\cdot\text{OH}$ species from the Co/Bi-1:6 photocatalysts was stronger than that from the pure $\text{Bi}_2\text{O}_2\text{CO}_3$, which indirectly explains the significance of introducing Co_3O_4 in the pure $\text{Bi}_2\text{O}_2\text{CO}_3$ and forming the p-n heterojunction. Based on the above results, it can be concluded that h^+ and $\cdot\text{OH}$ are the critical active species in the photodegradation system.

In order to clarify why the photocatalytic activity enhanced over the $\text{Co}_3\text{O}_4/\text{Bi}_2\text{O}_2\text{CO}_3$ photocatalyst, the band structure and density of states of $\text{Bi}_2\text{O}_2\text{CO}_3$ and Co_3O_4 were respectively calculated by density functional theory (DFT) in Fig. 9. It is well known that p-n heterojunction is a meaningful structure in favor of separation efficiency of electron-hole pairs which is a significant factor for photocatalytic efficiency. $\text{Bi}_2\text{O}_2\text{CO}_3$ is a relatively wide band-gap semiconductor with the band-gap energy of 3.142 eV (Fig. 9b), while Co_3O_4 has a relatively narrow band-gap energy of 2.27 eV (Fig. 9d). The calculated data are closed to the experimental values by DRS spectra. For $\text{Bi}_2\text{O}_2\text{CO}_3$, the conduction band (CB) edge is basically composed of Bi 6p, Bi 6s, and O 2p orbitals, while the valence band (VB) edge is mainly made up of Bi 6p, Bi 6s, O 2p, C 2p, and O 2s orbitals. The O atoms, adjacent C and Bi atoms are well hybridized in VB so that the VB electrons are difficult to be excited. It is owing to the fact that large hybrid electron density of O atoms with neighboring C and Bi atoms enhances electrostatic attraction between

the nuclear and electrons. At the same time, the lower hybrid electron density of Bi atoms with adjacent O atoms in the CB makes CB electrons easily migrate to the surface of $\text{Bi}_2\text{O}_2\text{CO}_3$, because it reduces electrostatic attraction between the nuclear and electrons. It also effectively avoids recombination of electron-hole pairs. Compared to $\text{Bi}_2\text{O}_2\text{CO}_3$, the CB edge of Co_3O_4 mainly consists of O 2s, Co 2p, and Co 3d orbitals, while the VB edge is basically composed of O 2p, O 2s, Co 4s, and Co 3d orbitals. O atoms with adjacent Co atoms have the low hybridization in the VB, implying that the VB electrons are easily to be excited. Nevertheless, due to the large hybrid electron density of Co atoms with O atoms nearby in the CB, the CB electrons mostly transfer inside the Co_3O_4 to cause high recombination of electron-hole pairs. Therefore, in the $\text{Co}_3\text{O}_4/\text{Bi}_2\text{O}_2\text{CO}_3$ hybrid photocatalyst system, the hybrid electron density in the CB of Co_3O_4 will be reduced, which favors to CB electrons transfer to the surface $\text{Bi}_2\text{O}_2\text{CO}_3$ and hampers recombination of electron-hole pairs. Meanwhile, the addition of Co_3O_4 forming the p-n heterojunction will also cause the reduction of hybrid electron density in the VB of $\text{Bi}_2\text{O}_2\text{CO}_3$. It is the benefit of VB electrons transferring into the CB. Therefore, the successful preparation of $\text{Co}_3\text{O}_4/\text{Bi}_2\text{O}_2\text{CO}_3$ composite can achieve efficient separation of electron-hole pairs and thus improve the photocatalytic performance of $\text{Co}_3\text{O}_4/\text{Bi}_2\text{O}_2\text{CO}_3$ hybrid photocatalysts.

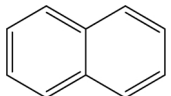
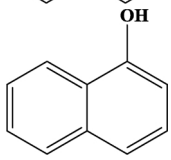
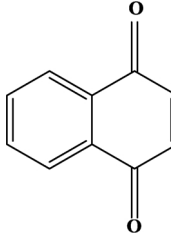
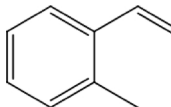
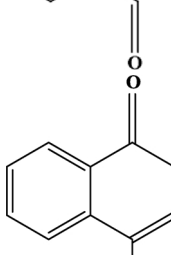
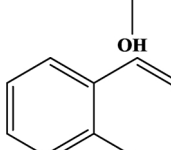
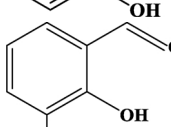
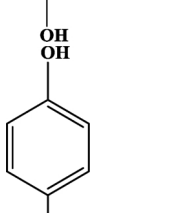
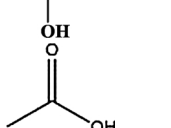
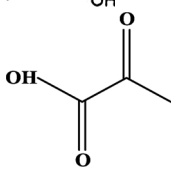
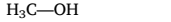
The proposed photocatalytic degradation mechanism and the schematic drawing of electron-hole separation process are figuratively depicted in Fig. 10. Co_3O_4 is a p-type semiconductor and $\text{Bi}_2\text{O}_2\text{CO}_3$ is an n-type semiconductor. Theoretically, when p-n heterojunction structure is formed between the p-type Co_3O_4 and the n-type $\text{Bi}_2\text{O}_2\text{CO}_3$, an inner electric field appears with a negatively charged section at the interface of the p-type Co_3O_4 region and with a positively charged portion at the interface of the n-type $\text{Bi}_2\text{O}_2\text{CO}_3$ region. Under the influence of an inner electric field, the holes transfer into the negative field while the electrons move to the positive field. The direction of an internal electric field is from $\text{Bi}_2\text{O}_2\text{CO}_3$ to Co_3O_4 . Thus, the photo-generated electrons and holes are separated efficiently, and the photocatalytic activity is enhanced. Moreover, the photocatalytic property of the photocatalyst is concerned with its band structure. The conduction band edge (E_{CB}) and valence band position (E_{VB}) of two semiconductors at the point of zero charges (pH_{ZPC}) can be predicted by the following Eqs. (4) and (5) [58]:

$$E_{\text{CB}} = X - E^e - \frac{1}{2}E_g \quad (4)$$

$$E_{\text{VB}} = E_{\text{CB}} + E_g \quad (5)$$

Where X is the absolute electronegativity of the semiconductor, E^e is the energy of free electrons on the hydrogen scale (4.5 eV), and E_g is the

Table 2
Identification of the degradation intermediates of NA by GC–MS.

Product	Retention time(min)	<i>m/z</i>	Name	Molecular structure
A	7.84		naphthalene	
B	12.12		α -naphthol	
C	10.99		1,4-naphthalenedione	
D	8.28		1,6-phthalaldehyde	
E	16.14		phthalic acid	
F	9.43		2-hydroxybenzaldehyde	
G	11.39		2,3-dihydroxybenzaldehyde	
H	7.03		Hydroquinone	
I	7.43		Acetic acid	
J	9.43		Oxalic acid	
K	11.39		Methanol	

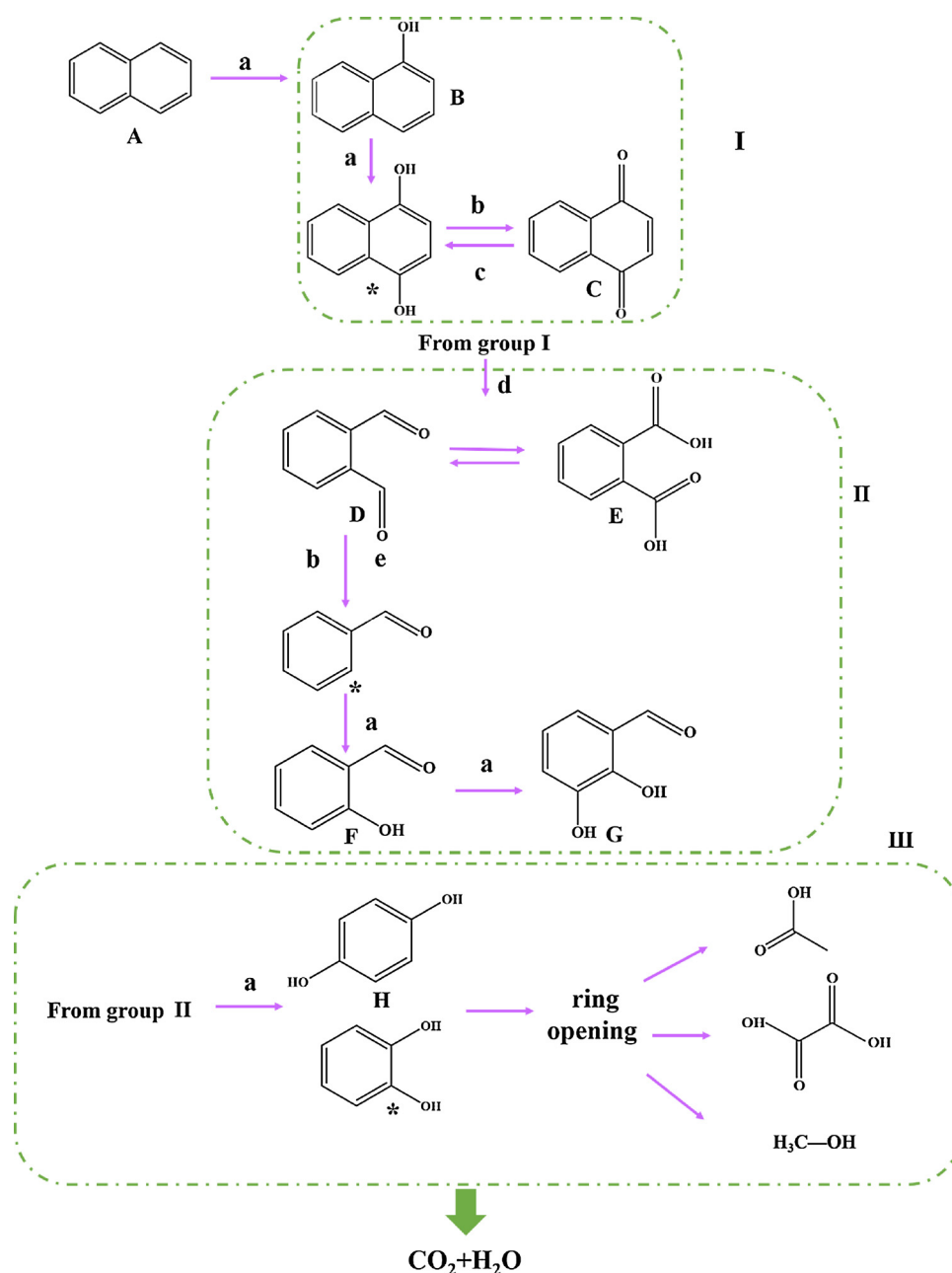


Fig. 11. Proposed NA degradation pathways on the Co/Bi-1:6.

band gap of the semiconductor. The position of the CB and the VB for $\text{Bi}_2\text{O}_2\text{CO}_3$ and Co_3O_4 crystallites, calculated according to the equation, are shown in Fig. 10. The E_{CB} values of $\text{Bi}_2\text{O}_2\text{CO}_3$ and Co_3O_4 are calculated to be 0.37 and 0.338 eV, respectively. The E_{VB} values of $\text{Bi}_2\text{O}_2\text{CO}_3$ and Co_3O_4 are estimated to be 3.43 and 2.468 eV, respectively. The calculated values are marginally larger than the measured values, but it does not affect the comparison of their relative positions.

Under the visible light irradiation, the electrons in the CB of the p-type Co_3O_4 can easily transfer to the n-type $\text{Bi}_2\text{O}_2\text{CO}_3$. The transformation orientation of holes is opposite, which in the VB of n-type $\text{Bi}_2\text{O}_2\text{CO}_3$ can transfer to the p-type Co_3O_4 . Thus, an effective separation of photoexcited electron-hole happens in p-n junction photocatalyst, which can be attributed to inner electric field assisted charge transfer at the junction interfaces between the semiconductors with matching band potentials, accordingly obtaining the enhancement of photocatalytic performance.

Moreover, the CB potential of $\text{Bi}_2\text{O}_2\text{CO}_3$ (0.37 eV) and Co_3O_4

(0.338 eV) is not negative enough compared with the standard reduction potential of $\text{O}_2/\cdot\text{O}_2^-$ (-0.33 eV), indicating that the large number of electrons on the surface of $\text{Bi}_2\text{O}_2\text{CO}_3$ could not be trapped by molecular oxygen in the solution reduced to $\cdot\text{O}_2^-$. Furthermore, the VB potentials of Co_3O_4 and $\text{Bi}_2\text{O}_2\text{CO}_3$ respectively are 2.468 and 3.43 eV, which are positive enough to oxidize the OH^- or H_2O into $\cdot\text{OH}$. Therefore, the most of h^+ on the surface of Co_3O_4 can oxidize OH^- or H_2O into $\cdot\text{OH}$. In addition, the partial h^+ from $\text{Bi}_2\text{O}_2\text{CO}_3$ can transfer OH^- or H_2O into $\cdot\text{OH}$ radicals. The proposed calculated results have also proved that h^+ and $\cdot\text{OH}$ radicals are the main reactive species in the photocatalytic degradation of NA.

The theoretical calculation of frontier electron densities (FED) was utilized to correctly predict the reaction sites for free radicals attack. According to Frontier Orbital Theory, the higher value of $\text{FED}_{\text{HOMO}}^2 + \text{FED}_{\text{LUMO}}^2$ presents that the position is more susceptible to be attacked by free radicals [59]. Based on the calculated data of NA (Fig. S2) in Table S1, in terms of $\text{FED}_{\text{HOMO}}^2 + \text{FED}_{\text{LUMO}}^2$, 3C, 6C, 7C, and 10C have the

highest values; 1C, 2C, 8C, and 9C have the relatively higher values, so these positions possess a fair chance of electron extraction. 4C and 5C have the relatively lower $FED_{HOMO}^2 + FED_{LUMO}^2$ values. The results provide the theoretical basis for the speculations of photocatalytic degradation pathways.

The formation and characterization of intermediates were identified by GC–MS. The photocatalytic products were analyzed based on the values of m/z and compared them with the U.S. National Institute of Standards and Technology (NIST) library. The chemical structures of the compounds detected by GC–MS along with their retention time and molecular weights are presented in Table 2. The transient species have been divided into three groups (Fig. 11).

The first group of compounds (I) accounts for the attack of reactive radicals (mainly $\cdot OH$, h^+) to the starting naphthalene (A) molecule. Hydroxylation reactions (path a) assumed as the initial events (path a). Due to the redox potential of the couple diol/quinone, the oxidation (path b) of diols to the corresponding quinones usually follows at a rate, the diols and quinones can achieve the interconversion. The hypothesized compound 1,4-dihydroxynaphthalene (not detected) can quickly transfer into (C) in the oxidizing reaction media, which causes its accumulation below the measurable concentration levels. In all the reactions observed in the group (I), the total number of carbon atoms of the intermediates remains constant. Further chemical processes (group II) must involve the above-mentioned derivatives. The opening of the oxidized rings combined with reduction/oxidation (path c & path b) and decarboxylation reactions (paths d) in compounds of the group (I) may bring to the formation of compounds (D) and (E) [60]. These two compounds might change from one to another through redox reactions (path b & path c). From compound (D), the formation of benzaldehyde (the hypothetical product) can also occur through an oxidation (path b)/decarboxylation (path e) step. The reaction that benzaldehyde was hydroxylated may explain the formation of the identified compounds (F) and (G). Oxidation and decarboxylation of aromatic substituents in compounds of the group II, coupled with hydroxylation (path a) of the benzene ring, may justify the formation of hydroquinone (H) and pyrocatechol (the hypothetical product) in the group III. The compounds are typical precursors of the ring opening, which leads to the formation of various aliphatic derivatives. Finally, they, in turn, go through oxidation and decarboxylation steps with the formation of CO_2 and H_2O as final products.

4. Conclusion

In summary, we developed a facile hydrothermal method to prepare p–n heterojunction photocatalyst $p-Co_3O_4/n-Bi_2O_2CO_3$ with 0D-2D nanocrystal/lotus-leaf-like nanosheet structure for the first time. Compare to the pure $Bi_2O_2CO_3$, the $Co_3O_4/Bi_2O_2CO_3$ heterojunction exhibited the higher photocatalytic degradation of naphthalene, especially the one with $Co_3O_4/Bi_2O_2CO_3$ mass ratio of 1:6 showed the highest photocatalytic performance of the pollutant with the degradation efficiency of about 91.02% naphthalene in 150 min, which could be attributed to the suppression of photogenerated charge carriers and the enhancement of light absorption. It was found that h^+ and $\cdot OH$ are the critical active species in the photodegradation system. Furthermore, 10 intermediates were identified by GC–MS during the process. The proposed reaction processes of photodegradation were discussed in detail combining the frontier electron density calculation and GC–MS results. The present study will be of great benefit to the development of the novel visible-light-driven p–n heterojunction nanocomposite with unique structure and may provide the possibility to tackle more environmental problems which are difficult to deal with in the future.

Acknowledgments

The authors greatly acknowledge the National Natural Science Foundation of China (No. 51578279), the National Major Project of

Science and Technology Ministry of China (Grant No. 015ZX07204-007-005) and the Shanghai Tongji Gao Tingyao Environmental Science & Technology Development Foundation (STGEF).

Appendix A. Supplementary data

Supplementary material related to this article can be found, in the online version, at doi:<https://doi.org/10.1016/j.apcatb.2018.05.089>.

References

- [1] D.F. Kalf, T. Crommentuijn, E.J. vandePlassche, *Ecotoxicol. Environ. Safe* 36 (1997) 89–97.
- [2] H.H. Soclo, P. Garrigues, M. Ewald, *Mar. Pollut. Bull.* 40 (2000) 387–396.
- [3] M.P. Zakaria, H. Takada, S. Tsutsumi, K. Ohno, J. Yamada, E. Kouno, H. Kumata, *Environ. Sci. Technol.* 36 (2002) 1907–1918.
- [4] S.C. Wilson, K.C. Jones, *Environ. Pollut.* 81 (1993) 229–249.
- [5] C.A. Menzie, B.B. Potocki, J. Santodonato, *Environ. Sci. Technol.* 26 (1992) 1278–1284.
- [6] S. Gan, E.V. Lau, H.K. Ng, *J. Hazard. Mater.* 172 (2009) 532–549.
- [7] M.R. Hoffmann, S.T. Martin, W.Y. Choi, D.W. Bahnemann, *Chem. Rev.* 95 (1995) 69–96.
- [8] H.H. Gan, G.K. Zhang, H.X. Huang, *J. Hazard. Mater.* 250 (2013) 131–137.
- [9] C. Srinivasan, N. Somasundaram, *Curr. Sci. India* 85 (2003) 1431–1438.
- [10] R.G. Li, F.X. Zhang, D.G. Wang, J.X. Yang, M.R. Li, J. Zhu, X. Zhou, H.X. Han, C. Li, *Nat. Commun.* 4 (2013).
- [11] T.W. Kim, K.S. Choi, *Science* 343 (2014) 990–994.
- [12] W.J. Jo, J.W. Jang, K.J. Kong, H.J. Kang, J.Y. Kim, H. Jun, K.P.S. Parmar, J.S. Lee, *Angew. Chem. Int. Ed.* 51 (2012) 3147–3151.
- [13] D.J. Mao, S.S. Ding, L.J. Meng, Y.X. Dai, C. Sun, S.G. Yang, H. He, *Appl. Catal. B: Environ.* 207 (2017) 153–165.
- [14] S. Ding, D. Mao, S. Yang, F. Wang, L. Meng, M. Han, H. He, C. Sun, B. Xu, *Appl. Catal. B: Environ.* 210 (2017) 386–399.
- [15] M.X. Ji, J. Di, Y.P. Ge, J.X. Xia, H.M. Li, *Appl. Surf. Sci.* 413 (2017) 372–380.
- [16] P. Madhusudan, J.R. Ran, J. Zhang, J.G. Yu, G. Liu, *Appl. Catal. B: Environ.* 110 (2011) 286–295.
- [17] L. Chen, R. Huang, S.F. Yin, S.L. Luo, C.T. Au, *Chem. Eng. J.* 193 (2012) 123–130.
- [18] X.H. Li, J.S. Chen, X.C. Wang, J.H. Sun, M. Antonietti, *J. Am. Chem. Soc.* 133 (2011) 8074–8077.
- [19] Y.M. He, L.H. Zhang, B.T. Teng, M.H. Fan, *Environ. Sci. Technol.* 49 (2015) 649–656.
- [20] T.Y. Zhao, J.T. Zai, M. Xu, Q. Zou, Y.Z. Su, K.X. Wang, X.F. Qian, *Crystengcomm* 13 (2011) 4010–4017.
- [21] L. Chen, S.F. Yin, S.L. Luo, R. Huang, Q. Zhang, T. Hong, P.C.T. Au, *Ind. Eng. Chem. Res.* 51 (2012) 6760–6768.
- [22] Z.Y. Zhao, Y. Zhou, F. Wang, K.H. Zhang, S. Yu, K. Cao, *ACS Appl. Mater. Interfaces* 7 (2015) 730–737.
- [23] H.F. Cheng, B.B. Huang, K.S. Yang, Z.Y. Wang, X.Y. Qin, X.Y. Zhang, Y. Dai, *Chemphyschem* 11 (2010) 2167–2173.
- [24] Y.Y. Liu, Z.Y. Wang, B.B. Huang, K.S. Yang, X.Y. Zhang, X.Y. Qin, Y. Dai, *Appl. Surf. Sci.* 257 (2010) 172–175.
- [25] Y. Zheng, F. Duan, M.Q. Chen, Y. Xie, *J. Mol. Catal. A Chem.* 317 (2010) 34–40.
- [26] L. Jin, G.Q. Zhu, M. Hojamberdiev, X.C. Luo, C.W. Tan, J.H. Peng, X.M. Wei, J.P. Li, P. Liu, *Ind. Eng. Chem. Res.* 53 (2014) 13718–13727.
- [27] S. Ida, A. Takashiba, S. Koga, H. Hagiwara, T. Ishihara, *J. Am. Chem. Soc.* 136 (2014) 1872–1878.
- [28] Y.N. Huo, X.F. Chen, J. Zhang, G.F. Pan, J.P. Jia, H.X. Li, *Appl. Catal. B: Environ.* 148 (2014) 550–556.
- [29] Y. Guo, J. Li, Z. Gao, X. Zhu, Y. Liu, Z. Wei, W. Zhao, C. Sun, *Appl. Catal. B: Environ.* 192 (2016) 57–71.
- [30] N. Liang, J.T. Zai, M. Xu, Q. Zhu, X. Wei, X.F. Qian, *J. Mater. Chem. A* 2 (2014) 4208–4216.
- [31] N. Tian, H.W. Huang, Y.X. Guo, Y. He, Y.H. Zhang, *Appl. Surf. Sci.* 322 (2014) 249–254.
- [32] N. Liang, M. Wang, L. Jin, S. Huang, W. Chen, M. Xu, Q. He, J. Zai, N. Fang, X. Qian, *ACS Appl. Mater. Interfaces* 6 (2014) 11698–11705.
- [33] L.H. Yu, X.Y. Zhang, G.W. Li, Y.T. Cao, Y. Shao, D.Z. Li, *Appl. Catal. B: Environ.* 187 (2016) 301–309.
- [34] H. Tuysuz, Y.J. Hwang, S.B. Khan, A.M. Asiri, P.D. Yang, *Nano Res.* 6 (2013) 47–54.
- [35] O. Yezhekel, D.R.B. de Oliveira, J.N. Cha, *Small* 11 (2015) 668–674.
- [36] S.K. Meher, G.R. Rao, *J. Phys. Chem. C* 115 (2011) 25543–25556.
- [37] X.W. Xie, Y. Li, Z.Q. Liu, M. Haruta, W.J. Shen, *Nature* 458 (2009) 746–749.
- [38] X.W. Lou, D. Deng, J.Y. Lee, J. Feng, L.A. Archer, *Adv. Mater.* 20 (2008) 258.
- [39] M. Long, W.M. Cai, J. Cai, B.X. Zhou, X.Y. Chai, Y.H. Wu, *J. Phys. Chem. B* 110 (2006) 20211–20216.
- [40] C.C. Han, L. Ge, C.F. Chen, Y.J. Li, X.L. Xiao, Y.N. Zhang, L.L. Guo, *Appl. Catal. B: Environ.* 147 (2014) 546–553.
- [41] D.D. Ma, J.W. Shi, Y.J. Zou, Z.Y. Fan, X. Ji, C.M. Niu, *ACS Appl. Mater. Interfaces* 9 (2017) 25377–25386.
- [42] F. Dong, Y.J. Sun, M. Fu, W.K. Ho, S.C. Lee, Z.B. Wu, *Langmuir* 28 (2012) 766–773.
- [43] W. Zhao, Y. Liu, Z.B. Wei, S.G. Yang, H. He, C. Sun, *Appl. Catal. B: Environ.* 185 (2016) 242–252.

- [44] P. Wang, L. Xu, Y. Ao, C. Wang, J. Colloid Interface Sci. 495 (2017) 122–129.
- [45] S. Xiong, J.S. Chen, X.W. Lou, H.C. Zeng, Adv. Funct. Mater. 22 (2012) 861–871.
- [46] F. Wang, Z. Zhao, K. Zhang, F. Dong, Y. Zhou, Crystengcomm 17 (2015) 6098–6102.
- [47] P. Madhusudan, J. Zhang, B. Cheng, G. Liu, Crystengcomm 15 (2013) 231–240.
- [48] L. Chen, S.-F. Yin, S.-L. Luo, R. Huang, Q. Zhang, T. Hong, P.C.T. Au, Ind. Eng. Chem. Res. 51 (2012) 6760–6768.
- [49] L. Zhou, W. Wang, L. Zhang, J. Mol. Catal. A Chem. 268 (2007) 195–200.
- [50] X. Zhang, T. Guo, X. Wang, Y. Wang, C. Fan, H. Zhang, Appl. Catal. B: Environ. 150 (2014) 486–495.
- [51] S. Vijayakumar, A.K. Ponnalagi, S. Nagamuthu, G. Muralidharan, Electrochim. Acta 106 (2013) 500–505.
- [52] Z. Wang, W. Guan, Y. Sun, F. Dong, Y. Zhou, W.-K. Ho, Nanoscale 7 (2015) 2471–2479.
- [53] K. Lv, X. Li, K. Deng, J. Sun, X. Li, M. Li, Appl. Catal. B: Environ. 95 (2010) 383–392.
- [54] J. Di, J. Xia, S. Yin, H. Xu, M. He, H. Li, L. Xu, Y. Jiang, RSC Adv. 3 (2013) 19624–19631.
- [55] P. Wang, Y. Ao, C. Wang, J. Hou, J. Qian, Carbon 50 (2012) 5256–5264.
- [56] X. Xiao, C. Xing, G. He, X. Zuo, J. Nan, L. Wang, Appl. Catal. B: Environ. 148 (2014) 154–163.
- [57] Z. Chen, W. Wang, Z. Zhang, X. Fang, J. Phys. Chem. C 117 (2013) 19346–19352.
- [58] H. Katsumata, T. Sakai, T. Suzuki, S. Kaneco, Ind. Eng. Chem. Res. 53 (2014) 8018–8025.
- [59] Y. Li, S. Yang, C. Sun, L. Wang, Q. Wang, Water Res. 88 (2016) 173–183.
- [60] J. Theurich, D.W. Bahnemann, R. Vogel, F.E. Ehamed, G. Alhakimi, I. Rajab, Res. Chem. Intermed. 23 (1997) 247–274.